

IDENTIFICATION OF PATTERNS OF THERMAL UNREST IN TAAL VOLCANO USING REMOTE SENSING

Jann Rovic Cueto, Ann Hera Quillope, Matthew Emmanuel Y. Alabado*

Department of Earth and Space Science, Rizal Technological University, Boni Mandaluyong – (2022-104684, 2022-103767, 2022-104515)@rtu.edu.ph

KEY WORDS: Thermal Unrest, Interferometry, Deformation Patterns, Remote Sensing, Volcano Activity.

ABSTRACT:

This study investigated the potential relationship between Land Surface Temperature (LST) and Displacement within the context of thermal unrest in Taal Volcano using remote sensing. We analyzed a dataset spanning several years to understand patterns of change and potential correlations between these variables. The results revealed a weak negative correlation between LST and Displacement, with a correlation coefficient of approximately -0.154 . However, the statistical analysis indicated that this correlation was not statistically significant. To improve future research in this area, we recommended the utilization of time series analysis to explore temporal trends, and the diversification of data sources, including information from various satellites. While our specific findings did not yield strong correlations, the study's outcomes contributed valuable insights into understanding thermal unrest in the Taal Volcano region using remote sensing, with a focus on LST and Displacement. Further research, incorporating these recommendations, will help our understanding of this complex relationship.

1. INTRODUCTION

Taal Volcano, situated in Batangas, Philippines, is an active caldera-type volcano, located in the tectonically complex Pacific Ring of Fire. The Philippines, characterized by numerous volcanoes and susceptibility to seismic events, necessitates a profound understanding of volcanic behavior for effective hazard assessment and risk management. This study is driven by the need to identify and comprehend patterns of thermal unrest in Taal Volcano, which pose a significant risk to nearby communities. To achieve this goal, we employ the cost-effective and efficient approach of analyzing thermal anomalies through satellite remote sensing technology (Coppola et al., 2020).

By examining the temporal variations in thermal activity, we aim to gain valuable insights into the volcano's behavior. In addition to thermal unrest, we recognize the importance of deformation analysis for comprehending volcanic processes and assessing volcanic hazards. Consequently, our investigation also delves into the deformation patterns within Taal Volcano using geodetic data derived from satellite observations. The combined analysis of thermal and deformation data through satellite remote sensing aims to enhance our understanding of the volcano's behavior and its potential for future volcanic activity. Understanding these patterns of thermal unrest and deformation is of utmost importance for early detection and mitigation of volcanic hazards. The timely identification of thermal anomalies and deformation signals can greatly assist authorities in implementing evacuation plans and taking necessary measures to protect vulnerable communities (Jiménez-Muñoz et al., 2009).

Through the utilization of satellite remote sensing data and geodetic analysis, our primary objective is to contribute to the body of knowledge related to volcanic activity and its underlying dynamics at Taal Volcano. While we employ

correlation analysis to understand the potential relationship between the two patterns, our primary goal is not prediction but to maximize the utility of remote sensing in monitoring the volcano's behavior. These insights will be invaluable for enhancing volcano monitoring and risk management strategies, ultimately contributing to the safety and well-being of communities residing near Taal Volcano.

2. MATERIAL AND METHODS

2.1. The Study Area

Taal Volcano's prominence in the geological landscape was attributed to its unique structural characteristics. It featured a large caldera with an approximate diameter of 25.7 kilometers, making it one of the world's most noteworthy calderas (Ramirez and Abdullah, 2022). This caldera enclosed Taal Lake, a substantial body of water that encompassed a diverse ecosystem. The lake's pristine waters and surrounding regions supported a variety of flora and fauna, and its ecological significance was widely recognized. Recent geological records highlighted a significant eruption that occurred in January 2020, leaving a profound impact on the region (Prasetyo et al., 2021). This eruption was characterized by phreatomagmatic activity, resulting from the interaction between magma and water. It culminated in a series of explosive volcanic events that had far-reaching consequences. The ash plume generated during the eruption reached considerable altitudes, affecting air traffic, and causing widespread ashfall across nearby towns and cities (Jing et al., 2020). The eruption prompted local authorities and researchers to intensify monitoring efforts to better understand the volcano's behavior and mitigate potential hazards. The study area, situated around Taal Volcano, also features unique topographical variations, with elevations ranging from the volcanic summit to the surrounding lowlands, contributing to microclimatic difference.

* Corresponding author

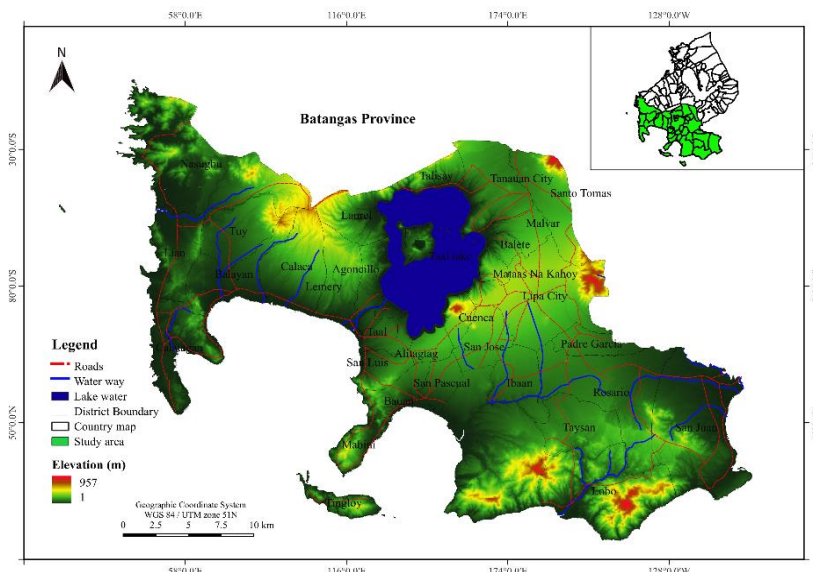


Figure 1. Location of the study area.

2.2. Data Processing

In our data processing, we implemented a rigorous methodology to quantitatively evaluate the correlations among the identified parameters. Our dataset encompassed various key components, including Land Surface Temperature (LST), deformation measurements derived from satellite imagery, and geodetic observations. A series of pre-processing steps was meticulously executed to refine and optimize the data quality, encompassing outlier removal, noise reduction, and data normalization. To address the non-normality observed in the data distribution, we applied robust statistical techniques, effectively mitigating the impact of extreme values and enhancing the trustworthiness of

our analyses. These measures empowered us to delve deeper into the relationships between LST variations and deformation patterns within the Taal Volcano region, ultimately aiding in developing a comprehensive understanding of its volcanic behavior.

2.2.1. Satellite Data

The satellite data utilized in this study spanned the period from 2019 to 2021, employing Landsat 8 OLI/TIRS and Sentinel 1 SAR platforms. For Landsat 8 OLI/TIRS (see Tab. 1), with a resolution of 30m and 100m, a swath width of 185km, and a revisit interval of 16 days, the study made use of 59 images.

Information	Details	Spatial Resolution
Product Name	LANDSAT/LC08/C01/T1_L2	
Date	2019-2021	
Path/Row	116/50, 116/51, 116/57, 116/ 59	
Ground Swath	185km	
Cloud Cover	0-25%	
Atmospheric Correction	B2, B3, B4, B5, B6	30m
NDVI	B5, B4	30m
Thermal	B10	100m

Table 1. Landsat-8 images including details used in the study.

The product name associated with this satellite data was "LANDSAT/LC08/C01/T1_L2." The data covered Path/Row 116/50, 116/51, 116/57, 116/ 59 and maintained a low cloud cover percentage ranging from 0 to 25%. To enhance the quality of the data, atmospheric correction was performed on bands B2, B3, B4, B5, and B6. The study focused on various spectral indices, such as NDVI (utilizing bands B5 and B4) and thermal data (band B10), to gain insights into land surface conditions. Due to some cloud cover in the images, we apply cloud masking on the images and use the monthly mean average land surface temperature each month which was used as data for correlation.

The Landsat 8 OLI/TIRS data were sourced from the USGS Earth Explorer. In Google Earth Engine, these data were accessed using the product name 'USGS Landsat 8 Level 2, Collection 2, Tier 1'. This specific product name facilitated the extraction of Landsat 8 images for our study. On the other hand,

the Sentinel 1 SAR data (see Tab. 2), featuring a resolution between 5m and 20m, a swath width of 250km, and a revisit interval of 6 days, comprised a total of 195 images. The beam mode was IW, and the polarization settings included VV and VH.

The data spanned Path 50-58, encompassing both ascending and descending directions, providing a comprehensive view of the study area. These Sentinel 1 SAR data were sourced from the LiCSAR portal, a machine learning platform that uses ESA Copernicus Sentinel - 1 data. LiCSAR significantly streamlines the analysis of time series InSAR data, making it an invaluable tool for extracting valuable insights and patterns from radar imagery collected over time (Lázecký et al., 2020). These satellite datasets were invaluable in the analysis and interpretation of various land surface characteristics, temporal changes, and geological phenomena over the study period. The

information was sourced from reputable references, ensuring data quality and reliability for the research. Sentinel -1 also used

monthly mean images and extract the values on the study area in used it to as the data points for correlation test.

Information	Details	Spatial Resolution
Product Name	L1 Single Look Complex	
Date	2019-2021	
Ground Swath	250km	
Beam Mode	IW	
Polarization	VV + VH	
Direction	Ascending and descending	
Band	C	5m – 20m
Frame Id	032D_07536_111313	

Table 2. Sentinel-1 images including details used in the study.

2.2.2. Satellite Data Processing

The study applied atmospheric correction to the Landsat images using the COST model (Chavez, 1996). This correction method involved utilizing the minimum band values to eliminate haze effects and converting the at-satellite radiance of all bands into surface reflectance. Top of Atmosphere (TOA) spectral radiance was calculated in the initial step, following an equation:

$$L_{\lambda} = M_L Q_{cal} + A_L \quad (1)$$

In this equation, L_{λ} represents the spectral radiance in watts/(m² srad⁻¹ μm⁻¹), M_L is the band-specific multiplicative rescaling factor obtained from the metadata (0.000342), A_L is the band-specific additive rescaling factor obtained from the metadata (0.1), and Q_{cal} is the DN value for the quantized and calibrated standard product pixel of band 10. The pre-processing and extraction of land surface temperature were conducted using the Google Earth Engine Geospatial platform. Subsequently, Land Surface Temperature (LST) was derived from the Landsat OLI/TIRS data band. The Brightness temperature was computed utilizing the original equation. To obtain the radiance value, it was then converted into Brightness Temperature (BT) using the following equation:

$$T_s = \frac{K_2}{\ln\left(\frac{K_1}{L_{\lambda}} + 1\right)} \quad (2)$$

In this equation, T_s represents the Brightness Temperature, and K_1 and K_2 are thermal conversion constants, which are detailed

Thermal constant	Band 10	Band 11
K1	777.89	480.89
K2	1321.08	1201.14

Table 3. K1 and K2 values.

The LiCSAR Sentinel-1 InSAR Processor, in conjunction with LiCSBAS, played a pivotal role in our research for constructing time series data related to volcano monitoring (Morishita et al., 2020). Our analysis started by accessing the Comet Volcano Portal, where we pinpointed our specific volcano of interest. Each volcano project corresponded to a distinct data frame ID, and in our study, we opted for frame number 032D_07536_111313. Once we selected the geographical area of interest, the platform seamlessly transitioned us to the interferometry machine learning environment. Here, we conducted data analysis effortlessly by manipulating interactive graphs, using slide bars to dissect the temporal displacement trends, and precisely defining our reference and target areas.

in Table 3 and can be in the metadata file of the Landsat image (Bendib et al., 2017). The formula is based on the methodology paper of another researcher (Rongali et al., 2018b). Emissivity, as defined in research studies is a fundamental radiative property of objects, indicating their ability to emit radiation (Rhinane et al., 2012). It plays a crucial role in the determination of surface temperature. To achieve this, a set of formulas for estimating emissivity for both urban and natural surfaces that are proposed in other research study was adapted (Meng and Li, 2019) and (Yang et al., 2014c).

For urban areas, the emissivity (E_{town}) was calculated using the formula:

$$\epsilon_{town} = 0.9608420 + 0.0860322P_v - 0.0671580P_v^2 \quad (3)$$

For natural surfaces, the emissivity ($E_{natural}$) was estimated using:

$$\epsilon_{natural} = 0.9643744 + 0.0614704P_v - 0.0461286P_v^2 \quad (4)$$

Furthermore, in these equations, P_v represents the vegetation proportion (Carlson and Ripley, 1997).

$$P_v = \left[\frac{NDVI - NDVI_s}{NDVI_v - NDVI_s} \right]^2 \quad (5)$$

The NDVI, which stands for Normalized Difference Vegetation Index, is computed as a ratio of two bands: near-infrared NIR and Red. The NDVI formula is expressed as:

$$NDVI = \frac{NIR - Red}{NIR + Red} \quad (6)$$

The system proved its robustness by automatically correcting delicate data points, enhancing the clarity of our data analysis. Upon concluding our analysis, we were able to extract the interferometry images. Subsequently, we tabulated the resulting data points efficiently using microsoft excel spreadsheet. Additionally, the Comet Volcano Portal offered a web-based analysis toolkit with clear instructions on how to evaluate potential deformation and changes (Anantrasirichai et al., 2018). Throughout our research, it was imperative to acknowledge and cite the pertinent sources while harnessing this potent tool for volcano monitoring (Morishita et al., 2020). This comprehensive approach facilitated the extraction of valuable insights for our volcano research and monitoring endeavours.

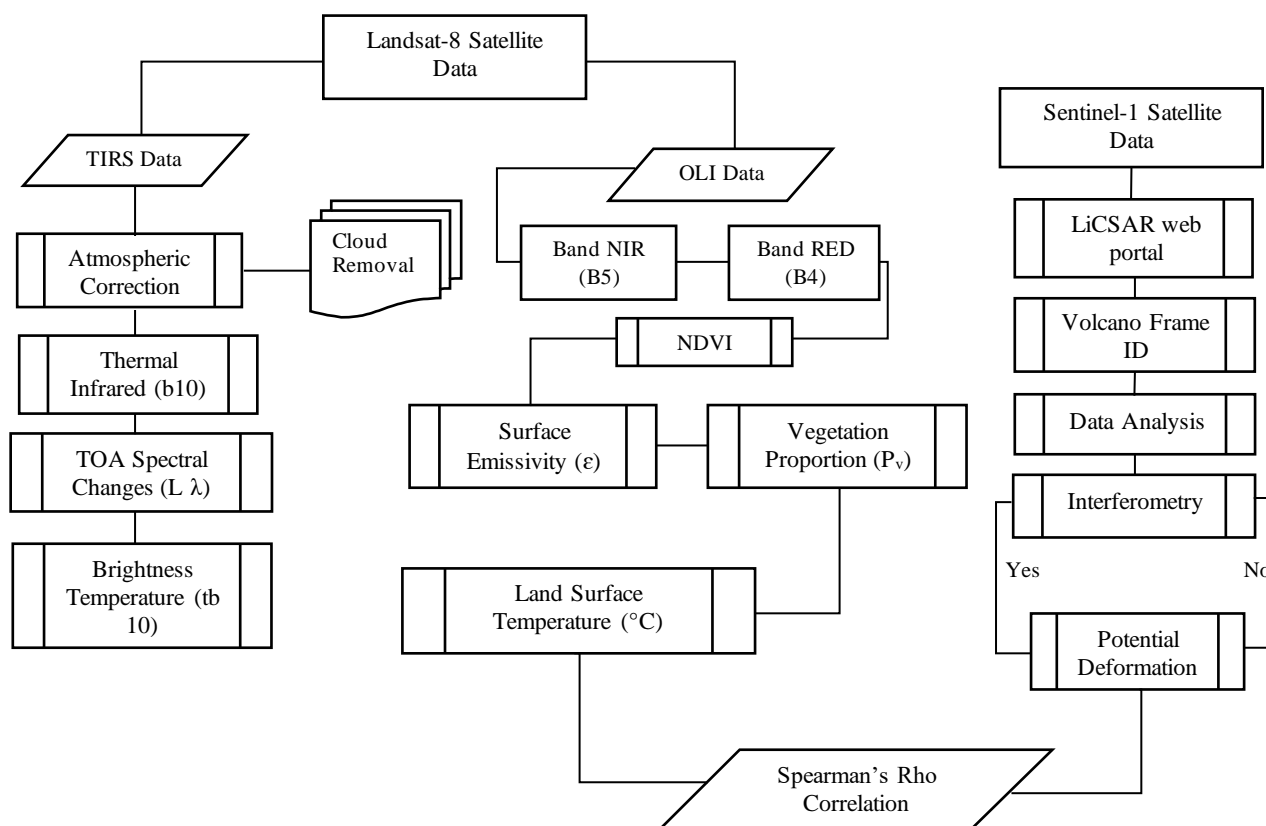


Figure 2. Flow chart of satellite data processing and analysis.

2.3 Statistics

In our research, we employed Spearman's rank correlation coefficient (Spearman's rho) as a fundamental non-parametric statistical method. This approach proved essential due to the non-normally distributed nature of the data we collected. By ranking the data, calculating differences between these ranks, and subsequently computing Spearman's rho, we could effectively assess the strength and direction of monotonic relationships between variables (Eden et al., 2021). Our choice of this statistical method was particularly valuable when exploring associations in cases where the data didn't adhere to normal distribution or were measured on ordinal scales. Certainly, Spearman's rank correlation coefficient (Spearman's rho) is determined by the formula:

$$\rho = 1 - \frac{6 \sum(d^2)}{N(N^2 - 1)} \quad (7)$$

where ρ represents the Spearman's rank correlation coefficient, d signifies the difference between the ranks of paired observations, and N is the total number of data points. This formula quantifies the strength and direction of the monotonic relationship between variables based on the ranks of the data (Eden et al., 2021).

2.3.1. Hypotheses

H_0 : There is no correlation between Land Surface Temperature and Displacement.

H_1 : There is a correlation between Land Surface Temperature and Displacement.

3. RESULTS AND DISCUSSIONS

In this section of the paper, we conduct an analysis and provide visual representations of cartographic and graphical data derived from datasets obtained through Landsat-8 and Sentinel-1 satellite platforms. These visual materials emphasize the consistent findings related to thermal activity in the Taal Volcano in the Philippines, which ultimately led to its eruption on January 12, 2020 (Bato et al., 2021). The use of these remote sensing satellites has resulted in harmonious observations, demonstrating parallel trends in thermal activity and deformation within the specified study area.

3.1. Land Surface Temperature

During its orbital trajectory and scan over the Taal volcano, the Landsat-8 Satellite accumulated data spanning both pre-eruption and post-eruption periods. In our research, we employed the Google Earth Engine to analyze Land Surface Temperature (LST) images. The year 2020 marked a significant turning point as a volcanic eruption generated a thermal anomaly within the volcano, which was vividly depicted in Figure 3. During this period, the images faced the substantial challenge of volcanic clouds. To overcome this challenge, we applied a masking technique to effectively filter out undesirable elements. Additionally, we overlaid the image acquired at the end of January, enabling us to calculate the mean average temperature. This calculation was pivotal in facilitating the extraction of LST data for each subsequent month, thereby providing us with comprehensive insights into temperature fluctuations over time. Notably, the images revealed a remarkable feature—the Taal region exhibited remarkable temperature spikes, with temperatures soaring beyond 40 degrees Celsius. In contrast, other regions maintained a more moderate temperature profile.

The significance of this specific image lay in its portrayal of the highest recorded maximum temperature throughout our three-year study period.

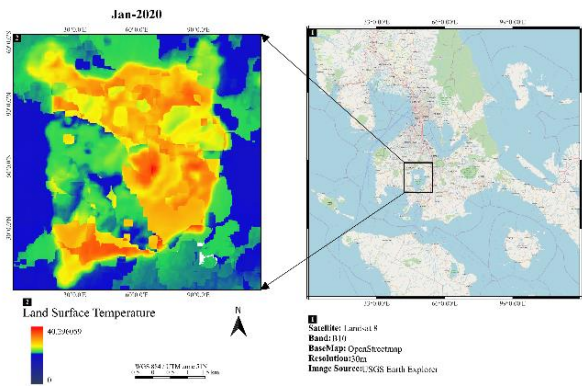


Figure 3. Land surface temperature in year 2020 captured by landsat-8.

3.2. Interferometry

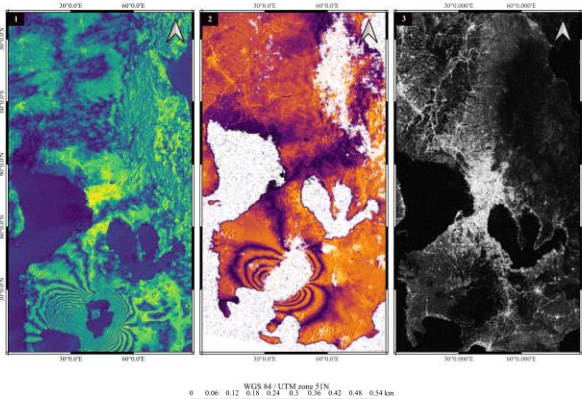


Figure 4. Interferometry images in year 2020 as the volcanic activity been more active.

The unwrapped line-of-sight (LOS) change wrapped LOS change, and coherence images (as shown in Fig. 4), delineated the formation of interferograms and coherence estimation within the designated area. These images helped to clarify the fringe patterns, which became visible after the interferogram was filtered to make the prominent fringes more noticeable. Particularly prominent in the upper region and partially in the lower region, these patterns resulted from the precise calculation of the distance between the satellite and the ground target. Fringes denoted incremental displacement indicative of deformation, with denser fringes correlating with greater deformation. It is essential to note that the images were captured within the timeframe of January 9 to January 15, 2020, effectively preceding the eruption that commenced on January 12. This temporal context was crucial, as it allowed us to comprehend the volcano's behavior leading up to the eruption event. The imagery encapsulated the dynamics of the Taal Volcano just prior to the eruption, providing a valuable snapshot of its pre-eruption state. This insight into the days preceding the eruption enhanced our understanding of the evolving conditions within the volcano and facilitated the identification of potential precursory signs. Furthermore, Figure

4 underscored the prevalence of dense fringes encircling Taal Volcano. The coherence image, a product of the conducted interferometry, served as a yardstick for gauging the quality of phase images produced. The coherence output, as observed in (Fig. 4), manifested as a gradient ranging from dark to light. Darker regions with low coherence lacked distinct fringes in the interferogram, while areas with higher coherence, indicated by lighter shades, exhibited clearer fringes. Furthermore, the initial sequence included Wrapped LOS change, Unwrapped LOS change, and coherence data as the satellite traversed the study area.

3.3. Correlational Analysis

In this study, we assessed two key variables, land surface temperature and ground displacement, to understand the data and determine the most suitable correlation method for addressing the research hypothesis. The descriptive statistics presented in the tables provided insights into the central tendencies and distribution characteristics of these parameters. Regarding Land Surface Temperature (see Table. 4), the dataset consisted of 36 data points. The mean Land Surface Temperature was found to be approximately 18.82°C, giving an estimate of the central value. The standard deviation, at 8.42, indicated the extent of variability in the temperature data. With a negative kurtosis value of -1.49, the distribution was considered platykurtic, having lighter tails and a less pronounced peak than a normal distribution. A positive skewness value of 1.18 pointed to a positively skewed distribution, indicating a longer right tail and a concentration of lower values on the left side. Notably, the Shapiro-Wilk Test revealed a p-value of 0.00000382, signifying a significant departure from normal distribution, suggesting non-normality in the data. As for Ground Displacement (see Table. 5), the dataset also comprised 36 data points. The mean Displacement was around 76.98, representing the central value. The standard deviation, at 49.13, indicated a moderate degree of variability.

The kurtosis value of -0.03 indicated a distribution nearly mesokurtic, with tails and peakness like a normal distribution. However, a negative skewness value of -1.15 suggested a negatively skewed distribution, characterized by a longer left tail and a concentration of higher values on the right side. The Shapiro-Wilk Test, with a p-value of 0.09, indicated a departure from normal distribution, although less pronounced than in the case of Land Surface Temperature. Additionally, the Kolmogorov-Smirnov Test, with a p-value of 0.19, suggested a deviation from normality. In summary, both Land Surface Temperature and Displacement data exhibited non-normal distributions, skewness, and kurtosis characteristics. Understanding these distribution properties is vital for informed statistical analysis and modelling decisions related to these parameters. In our research, we conducted a hypothesis test to investigate the relationship between Land Surface Temperature and Displacement. We formulated a null hypothesis (H0) stating that there is no correlation between these two variables and an alternative hypothesis (H1) suggesting the presence of a correlation. The results showed (see Table. 6) that the correlation coefficient between Displacement and Land Surface Temperature was approximately -0.154, indicating a weak negative correlation. However, the p-value associated with this correlation was 0.369. Since this p-value exceeded our chosen significance level of 0.05 (2-tailed), we could not find enough evidence to reject the null hypothesis. In simpler terms, our analysis did not provide strong support for a significant correlation between Land Surface Temperature and Displacement.

Descriptive Statistics

	Land Surface Temperature °C			
	statistic	std. error	z-values	p-value
N	36			
Mean	18.82	1.40		
Standard Deviation	8.42			
Kurtosis	-1.49	0.39	-3.79	
Skewness	1.18	0.77	1.53	
Shapiro-Wilk				0.00000382
Kolmogorov-Smirnov				0.00020484

Note: Significance level is set to >0.05.

Table 4. Land surface temperature descriptive statistics.

Descriptive Statistics

	Ground Displacement (mm)			
	statistic	std. error	z-values	p-value
N	36			
Mean	76.98	8.19		
Standard Deviation	49.13			
Kurtosis	-0.03	0.39	-0.07	
Skewness	-1.15	0.77	-1.50	
Shapiro-Wilk				0.09
Kolmogorov-Smirnov				0.19

Note: Significance level is set to >0.05.

Table 5. Ground displacement descriptive statistics.

Non -Parametric Correlations

	Spearman's rho				
	correlation coefficient	p-value	H ₀	H ₁	result
Displacement vs. Land Surface Temperature	-0.154	0.369	Not Rejected	Not Accepted	Weak negative Correlation

Note: Significance level is 0.05 (2-tailed).

Table 6. Spearman's rho correlation coefficient results.

4. CONCLUSION

This study conducts a statistical analysis to investigate the potential relationship between Land Surface Temperature and Displacement in the study area. The study formulates hypotheses to explore whether there is a correlation between these two variables. The results of the analysis indicate a weak negative association between Land Surface Temperature and Displacement, with a correlation coefficient of approximately -0.154. However, the p-value associated with this correlation was 0.369, which was not statistically significant. Therefore, based on the analysis, the study could not confirm the presence of a meaningful correlation between Land Surface Temperature and Displacement in the study area. In other words, changes in Land Surface Temperature are not likely to be substantially linked to changes in Displacement as suggested by the data.

These findings indicate that other factors or influences may be affecting Displacement. Further research or additional variables need to be explored to better understand this relationship. Incorporating additional data types such as sulfur dioxide and wind direction, and utilizing satellite data with higher revisit times, may provide more insights into the relationship between Land Surface Temperature and Displacement. Landsat's high resolution makes it sensitive to cloud cover, so alternative satellite data sources may prove to be beneficial.

ACKNOWLEDGEMENT

We wish to express our heartfelt appreciation to the experts who generously provided their valuable feedback and insights on our paper. Furthermore, we extend our acknowledgments to the LiCSAR open-source portal, which was instrumental in providing the Sentinel-1 InSAR data used in our research. Additionally, we recognize the USGS Earth Explorer for granting access to the Landsat-8 data that was essential for our study.

REFERENCES

Anantrasirichai, N., Biggs, J., Albino, F., Hill, P., & Bull, D., 2018. Application of machine learning to classification of volcanic deformation in routinely generated InSAR data. *Journal of Geophysical Research: Solid Earth*, 123(8), 6592–6606. doi.org/10.1029/2018jb015911.

Bato, M., Lundgren, P., Pinel, V., Solidum, R., Daag, A., Cahulogan, M., 2021. The 2020 eruption and large lateral dike emplacement at Taal Volcano, Philippines: Insights from satellite radar data. *Geophysical Research Letters*, 48(7). doi.org/10.1029/2021gl092803.

Bendib, A., Dridi, H., & Kalla, M., 2017. Contribution of Landsat 8 data for the estimation of land surface temperature in

- Batna city, Eastern Algeria. *Geocarto International*, 32(5), 503–513. doi.org/10.1080/10106049.2016.1156167.
- Carlson, T. N., Ripley, D. A., 1997. On the relation between NDVI, fractional vegetation cover, and leaf area index. *Remote Sensing of Environment*, 62(3), 241–252. doi.org/10.1016/s0034-4257(97)00104-1.
- Chavez, P. S., 1996. Image-based atmospheric corrections-revisited and improved. *Photogrammetric engineering and remote sensing*, 62(9), 1025-1035.
- Coppola, D., Laiolo, M., Cigolini, C., Massimetti, F., Donne, D. D., Ripepe, M., Arias, H., Barsotti, S., Parra, C. B., Quico, R. C., Cevuard, S., Chigna, G., Chun, C., Garaebiti, E., Gonzales, D. V., Griswold, J. P., Juarez, J., Lara, L. E., López, C., William, R. G., 2020. Thermal remote sensing for global volcano monitoring: experiences from the MIROVA system. *Frontiers in Earth Science*, 7. doi.org/10.3389/feart.2019.00362.
- Eden, S. K., Li, C., Shepherd, B. E., 2021. Nonparametric estimation of Spearman's rank correlation with bivariate survival data. *Biometrics*, 78(2), 421–434. doi.org/10.1111/biom.13453.
- Jiménez-Muñoz, J. C., Cristóbal, J., Sobrino, J. A., Sòria, G., Ninyerola, M., Pons, X., 2009. Revision of the Single-Channel Algorithm for land Surface Temperature Retrieval from Landsat Thermal-Infrared Data. *IEEE Transactions on Geoscience and Remote Sensing*, 47(1), 339–349. doi.org/10.1109/tgrs.2008.2007125.
- Jing, F., Chauhan, A., Singh, R. P., Dash, P., 2020. Changes in Atmospheric, Meteorological, and Ocean Parameters Associated with the 12 January 2020 Taal Volcanic Eruption. *Remote Sensing*, 12(6), 1026. doi.org/10.3390/rs12061026.
- Lázecký, M., Spaans, K., González, P. J., Maghsoudi, Y., Morishita, Y., Albino, F., Elliott, J. R., Greenall, N., Hatton, E., Hooper, A., Juncu, D., McDougall, A., Walters, R. J., Watson, C. S., Weiss, J., Wright, T., 2020. LICsAR: An Automatic InSAR Tool for Measuring and Monitoring Tectonic and Volcanic Activity. *Remote Sensing*, 12(15), 2430. doi.org/10.3390/rs12152430.
- Meng, C., Li, H., 2019. Assimilating Satellite Land Surface States Data from Fengyun-4A. *Scientific Reports*, 9(1). doi.org/10.1038/s41598-019-55733-3.
- Morishita, Y., Lázecký, M., Wright, T., Weiss, J., Elliott, J. R., Hooper, A., 2020. LiCSBAS: An Open-Source InSAR Time Series Analysis Package Integrated with the LiCSAR Automated Sentinel-1 InSAR Processor. *Remote Sensing*, 12(3), 424. doi.org/10.3390/rs12030424.
- Prasetyo, Y. T., Kurata, Y., Acosta, A. R., Aben, A. P. F. B., Persada, S. F., Nadlifatin, R., Redi, A. a. N. P., 2021. Factors affecting response actions of the 2020 Taal Volcano eruption among Filipinos in Luzon, Philippines: A structural equation modeling approach. *International Journal of Disaster Risk Reduction*, 63, 102454. doi.org/10.1016/j.ijdr.2021.102454.
- Ramirez, R., Abdullah, R., 2022. Damaged Area Mapping and Ground Displacement Estimation using Sentinel-1 Synthetic Aperture Radar (SAR) Interferometry: January 12, 2020, Taal Volcano Eruption Case Study, Philippines. *Mindanao Journal of Science and Technology*, 20(2). doi.org/10.61310/mndjsteect.1149.22.
- Rhinane, H., Hilali, A., Bahi, H., Berrada, A., 2012. Contribution of Landsat TM data for the detection of Urban Heat Islands Areas Case of Casablanca. *Journal of Geographic Information System*, 04(01), 20–26. doi.org/10.4236/jgis.2012.41003.
- Rongali, G., Keshari, A. K., Gosain, A. K., Khosa, R., 2018. Split-Window algorithm for retrieval of land surface temperature using Landsat 8 thermal infrared data. *Journal of Geovisualization and Spatial Analysis*, 2(2). doi.org/10.1007/s41651-018-0021-y.
- Yang, L., Cao, Y., Zhu, X., Zeng, S., Yang, G., He, J., Xiao, Y., 2014. Land surface temperature retrieval for arid regions based on Landsat-8 TIRS data: a case study in Shihezi, Northwest China. *Journal of Arid Land*, 6(6), 704–716. doi.org/10.1007/s40333-014-0071-z.